Collisional history of Ryugu's parent body from bright surface boulders

E. Tatsumi, C. Sugimoto, L. Riu, S. Sugita, T. Nakamura, T. Hiroi, T. Morota, M. Popescu, T. Michikami, K. Kitazato, et al.

Collisional history of Ryugu's parent body from bright surface boulders

Authors: E. Tatsumi[1,2,*], C. Sugimoto[2], L. Riu[3], S. Sugita[2], T. Nakamura[4], T. Hiroi[5], T. Morota[2], M. Popescu[1,6], T. Michikami[7], K. Kitazato[8], M. Matsuoka[3], S. Kameda[9], R. Honda[10], M. Yamada[11], N. Sakatani[3], T. Kouyama[12], Y. Yokota[3,9], C. Honda[7], H. Suzuki[13], Y. Cho[2], K. Ogawa[14], M. Hayakawa[3], H. Sawada[3], K. Yoshioka[2], C. Pilorget[16], M. Ishida[8], D. Domingue[17], N.Hirata[13] , S. Sasaki[18], J. de León[1], M. A. Barucci[19], P. Michel[20], M. Suemitsu[21], T. Saiki[3], S. Tanaka[3,15], F. Terui[3], S. Nakazawa[3], S. Kikuchi[3], T. Yamaguchi[3,†], N. Ogawa[3], G. Ono[22], Y. Mimasu[3], K. Yoshikawa[22], T. Takahashi[3], Y. Takei[3], A. Fujii[3], Y. Yamamoto[3,15], T. Okada[3,2], C. Hirose[22], S. Hosoda[3], O. Mori[3], T. Shimada[3], S. Soldini[23], R. Tsukizaki[3], T. Mizuno[3,15], T. Iwata[3,15], H. Yano[3,15], M. Ozaki[3,15], M. Abe[3,15], M. Ohtake[3,15], N. Namiki[24,15], S. Tachibana[25,3], M. Arakawa[13], H. Ikeda[22], M. Ishiguro[26], K. Wada[10], H. Yabuta[27], H. Takeuchi[3,15], Y. Shimaki[3], K. Shirai[3], N. Hirata[7], Y. Iijima[§], Y. Tsuda[3,15], S. Watanabe[21,3], M. Yoshikawa[3,15]

1. Instituto de Astrofísica de Canarias (IAC) and Department of Astrophysics, University of La Laguna, La Laguna, Tenerife, Spain.
2. The University of Tokyo, Bunkyo, Tokyo, Japan.
3. Institute of Space and Astronautical Science (ISAS), Japan Aerospace Exploration Agency (JAXA), Sagamihara, Kanagawa, Japan.
4. Tohoku University, Sendai, Miyagi, Japan.
5. Brown University, Providence, RI, USA.
6. Astronomical Institute of the Romanian Academy, Bucharest, Romania.
7. Kindai University, Higashi-Hiroshima, Hiroshima, Japan.
8. The University of Aizu, Aizu-Wakamatsu, Fukushima, Japan.
9. Rikkyo University, Toshima, Tokyo, Japan.
10. Kochi University, Kochi, Kochi, Japan.
11. Planetary Exploration Research Center (PERC), Chiba Institute of Technology, Narashino, Chiba, Japan.
12. National Institute of Advanced Industrial Science and Technology (AIST), Koto, Tokyo, Japan.
13. Meiji University, Kawasaki, Kanagawa, Japan.
14. Kobe University, Kobe, Hyogo, Japan.
15. SOKENDAI (The Graduate University for Advanced Studies), Hayama, Kanagawa, Japan.
16. Institut d'Astrophysique Spatiale, Orsey, France.
17. Planetary Science Institute, Tucson, AZ, USA.
18. Osaka University, Toyonaka, Osaka, Japan.
19. LESIA-Observatoire de Paris, Université PSL, CNRS, Sorbonne Université, Université Paris-Diderot, Sorbonne Paris Cité, Meudon, France.
20. Université Côte d'Azur, Observatoire de la Côte d'Azur, CNRS, Laboratoire Lagrange, Nice, France.
21. Nagoya University, Nagoya, Aichi, Japan.
22. Research and Development Directorate, JAXA, Sagamihara, Kanagawa, Japan.
23. University of Liverpool, Liverpool, UK.
24. National Astronomical Observatory of Japan, Mitaka, Tokyo, Japan.
26. Seoul National, University, Seoul, Korea.
27. Hiroshima University, Higashi-Hiroshima, Hiroshima, Japan.

[*]Corresponding author (E-mail: etatsumi@iac.es)
[†]Current affiliation: Mitsubishi Electric Corporation, Kamakur, Kanagawa, Japan.
[§]Deceased

Summary Paragraph (201 words excluding references)

(162173) Ryugu and other rubble-pile asteroids are likely re-accumulated fragments of much larger parent bodies that were disrupted by impacts. However, the collisional and orbital pathways from the original parent bodies to sub-kilometer rubble-pile asteroids are not yet well understood [1,2,3]. Here, we use Hayabusa2 observations to show that some of the bright boulders on the dark, carbonaceous ("C-type") asteroid Ryugu [4] are remnants of an impactor with a different composition as well as an anomalous portion of its parent body. The bright boulders on Ryugu can be classified into two spectral groups: most are featureless and similar to Ryugu's average spectrum [4,5], while others show distinct compositional signatures consistent with ordinary chondrites—a class of meteorites that originate from anhydrous-silicate-rich asteroids [6]. The observed anhydrous silicate-like material is likely the result of collisional mixing between Ryugu's parent body and one or multiple anhydrous-silicate-rich asteroid(s) before and during Ryugu's formation. In addition, the bright boulders with featureless spectra and less ultraviolet upturn are consistent with thermal metamorphism of carbonaceous meteorites [7,8]. They might sample a different thermal-metamorphosed regions, which the returned sample will allow us to verify. Hence, the bright boulders on Ryugu provide new insights into the collisional evolution and accumulation of sub-kilometer rubble-pile asteroids.

Main text (1793 words excluding references)

The near-Earth asteroids, Itokawa, Bennu, and Ryugu are rubble-pile asteroids that were formed by the gravitational re-accumulation of rock fragments made by collisional disruption of their parent body [1,2,3]. Asteroids are classified in two main spectral groups: 1) S-types, which are suggested to be composed of anhydrous-silicate-rich materials, and 2) C-types, which contain more carbon and hydrated minerals [9]. The delivery of organics and volatiles from the main asteroid belt has been hypothesized to explain the presence of the oceans and life on the Earth [10,11]. However, the transformation and mixture of materials from the main belt to the Earth crossing orbits is not well understood. Studies of exogenic matter on asteroids can provide some insight on the characteristics of catastrophic disruption of individual asteroids, such as projectile types and impact conditions. Here we report the discovery of bright boulders and discuss the implications on the history of material mixing on Ryugu.

JAXA's Hayabusa2 spacecraft started its investigation of (162173) Ryugu in June 2018 [2]. The initial global observations of Ryugu with the telescopic optical navigation camera ONC-T with seven broad band filters ranging from 0.40 to 0.95 μm have revealed that Ryugu's surface is uniformly dark (the geometric albedo is 4.5% at 0.55 μm) suggesting a thermally metamorphosed carbonaceous chondrite composition [4]. Similarly, Ryugu's near-infrared spectra are uniformly flat and low in reflectance with a weak absorption at 2.7 μm corresponding to a hydroxyl absorption, which is also consistent with heated carbonaceous chondrites [5]. After the initial global observations of Ryugu, Hayabusa2 conducted several high-resolution observations during proximity operations. As the spacecraft approached the surface, we resolved smaller structures in the ONC-T images, discovering numerous bright boulders at smaller scale (Fig. 1 and Extended Figure 1). Because of the uniformly dark nature of Ryugu, anomalous bright boulders on the surface are potentially exogenic material, which were first reported in the initial observations [4]. Because mostly they are smaller than 10 m, however, spectral

characterizations have not been previously conducted and their compositions were not discussed in the initial analyses.

We identified bright boulders as areas with peak normal albedo values >1.5 times brighter than Ryugu's globally averaged albedo, which corresponds to a peak normal albedo of >6.8% [Method 1], while the standard deviation in normal albedo is 4.1 – 5.0%. Bright boulders in high-resolution images exhibit inhomogeneous surface brightness (Fig. 1). The presence of fine dust covering the brighter layer, as observed during the touch-down operations [12], or different degree of space weathering [13] on different boulder parts due to possible motion and cracking could explain the variability in surface brightness. Figure 1(e) shows the cumulative size distribution of the bright boulders found in high-resolution images (down to 6 mm/pix) taken during the rover MINERVA-II deployment operation. The size distribution of boulders is expressed as $N(>D) \propto D^{-\alpha}$, where D is the boulder diameter and α is the power-law index. The power-law index $\alpha > 2$ is estimated for the bright boulders in each image [Extended Figure 7], which is similar to the entire boulder distribution in the same images [14]. The power-law index of $\alpha > 2$ is compatible with laboratory impact fragments, suggesting that the bright boulders were produced by catastrophic disruption rather than cratering [15]. The ratio between the distribution of bright boulders and all boulders including bright boulders [14] suggests a surface area ratio for bright boulders of ~0.03 – 1% [Method 2].

Using ONC-T multiband images taken on 3 to 4 October 2018 at an altitude of ~3 km (~0.3 m/pixel), the visible spectra of 21 bright boulders (M1 - M21) are examined [Extended Figure 2]. The spectra of bright boulders are classified into two groups depending on the presence or absence of an absorption towards 1 μm [Supplementary Information], which is indicative of the presence of silicates; Six out of 21 bright boulders show the mafic-silicate-like absorption (S-type bright boulders; Fig. 2), while the rest are featureless at 1 μm (C- or X-type bright boulders) [16]. The majority of bright boulders have featureless spectral shapes categorized into C/X-types. The spectral trend is continuous with the global spectra of Ryugu, suggesting that C/X-type bright boulders may not be exogenous but an original constituent of Ryugu or its parent body, despite the higher than average albedo. All the C/X-type bright boulders have less upturn towards ul band (0.40 μm), while the average spectrum shows strong upturn in shorter wavelengths. Because the visible to near-infrared spectrum of Ryugu suggests compatibility with thermally metamorphosed carbonaceous chondrites [4,5], It is important to discuss if the spectral variety in C/X-type bright boulders can be explained by an endogenic process. The spectral shapes of the C/X-type bright boulders are compared with laboratory heating experiments on the hydrated carbonaceous chondrites Murchison and Ivuna [7,8] (Fig. 3). Comparisons are made in the spectral slope from 0.55 to 0.86 μm and the degree of upturn in ultraviolet (UV index) space. During the heating of hydrous carbonaceous chondrites, the UV index first increases until 600 – 700 ˚C. This is due to the decomposition of hydrated phases and carbonization/graphitization of carbonaceous material. The UV index then decreases by formation of Fe-bearing secondary olivine and small FeNi metal particles and a decrease in carbon abundance by oxidation [17,18]. These spectral characteristics suggest a possible connection between the different spectral features of bright boulders and different degrees of thermal metamorphism. More specifically, the overall direction and range of spectral variation observed among C/X-type bright boulders in the UV-index/spectral slope space can be reproduced by those heating experiments. It is noted, however, that specific meteorite types or metamorphism temperatures cannot be determined solely based on the spectra. The C/X-type bright boulders may have experienced different thermal histories in the parent body

through heating by decay of short-lived radionuclide ^{26}Al [19] or/and impact [4]. Those C/X-type bright boulders could be sampled from different parts of the parent body during its catastrophic disruption and subsequent re-accumulations. The returned sample analyses will provide us strong constraints on this senario.

The normal albedos of S-type bright boulders range between 9 – 22%, while those of C/X-type bright boulders range between 5 – 10% [Extended Figure 6]. The average geometric albedo of S-type asteroids is 22.3 ± 7.3% and that of V-types is 36.2 ± 10.0% [20], supporting the designation that S-type bright boulders are similar to S-type asteroids regarding albedo. Large difference in spectrum and albedo suggest the S-type bright boulders are exogeneous material. The spectra of S-type bright boulders overlap with both ordinary chondrite (OC) and Howardite-Eucrite-Diogenite meteorite (HED) spectra. Furthermore, because both HEDs and OCs display a wide range of spectral variations in this visible color range, near-infrared spectral information is necessary for placing compositional constraints on them. Although near-infrared spectrometer NIRS3 also observed the S-type bright boulders, due to the larger footprint compared with the size of the bright boulders, we examined linear mixture of meteorite spectra with the average spectrum of Ryugu to compare meteorite spectra with the NIRS3 observations. The mixture is comprised of 99% the average Ryugu spectrum and 1% of the meteorite spectrum to mimic the footprint area covered by the bright boulder. To clarify any absorption caused by the bright boulders, the spectrum including the bright boulder is normalized by the spectrum of an adjacent area. After this normalization, the 2-μm band depth is measured [Method 3]. The linearly mixed spectra with HEDs display a 2-μm feature with a 2.5 ± 1.0% absorption, while the mixed spectra with the OCs display a 2-μm feature with 0.6 ± 0.3% absorption (Fig. 4). The bright boulders' band characteristics are consistent with either OCs or HEDs, although bright boulders do not present a strong 2 μm band absorption. Considering the albedo values and the small or no 2-μm band absorption, they are more spectrally similar to olivine-rich OCs. Those S-type bright boulders could originate from S-type asteroids, because S-type asteroids are the most abundant in the inner asteroid main belt [21] where Ryugu may have originated [22]. Moreover, more than half of the Nysa-Polana complex, which is Ryugu's likely source family [4], is populated by S-type members with similar orbital elements to C-type members [23]. Thus, the collisional mixture between C- and S-type asteroids inside the Nysa-Polana complex is highly likely.

Possible origins for the S-type exogenous materials on Ryugu are: 1) they are remnants from the collision at the origin of Ryugu between its parent body and anhydrous-silicate-rich asteroid(s) in the main belt, or 2) they landed at small relative velocity during Ryugu's subsequent orbital evolution. To examine the probability of these hypotheses, comparisons are made with the impact statistical estimates. Four to six S-type bright boulders >0.5 m in diameter have been found in the search area, covering ~40% of the entire surface. For an OC-like boulder to land on the surface without disruption requires the collision speed < 0.2 km/s [Method 4]. For 10 to 15 projectiles >0.5 m in diameter to collide Ryugu at <0.2 km/s , 10000 – 15000 of similar-sized asteroids including 2 - 8 projectiles 23 – 28 m in diameter would also hit Ryugu. This estimate is based on the mean impact velocity distribution between the main-belt asteroids [24] and the exponent of -2.55 for the cumulative size distribution of main-belt asteroids [25]. A projectile of 23 – 28 m is about the critical size of an impactor to disrupt Ryugu catastrophically (assuming the catastrophic disruption threshold, which is the specific energy required to disperse the targets into pieces smaller than the half mass of the original mass, Q_D^*~800 J/kg, [26]). The soft landing (e.g., ≤0.2 km/s) of several meter-

sized objects, during which the impactor does not break up, is much less frequent than the collision of 25-m-sized objects, which would catastrophically disrupt a 1-km body. Thus, all the S-type bright boulders cannot be accreted on Ryugu's surface well after the asteroid was formed; they had to be incorporated in Ryugu's parent body during its catastrophic disruption or before. Furthermore, for a fixed impact speed, a catastrophic disruption event of a larger body involves a larger fraction of projectile, which favors survived exogenic materials since the projectile/target mass ratio of a catastrophic disruption event is larger (i.e., a larger Q_D^*) for a larger target [26].

Overall, the bright boulders with different spectral types might constitute a witness of the collision between the parent body of Ryugu and one or multiple anhydrous-silicate-rich asteroid(s) that led to the formation of Ryugu. Even though several similarities have been discussed between Ryugu and Bennu, such as the region of origin in the main belt [24,27], albedo, and thermal inertia [3,4], the discovery that many of bright boulders on Bennu and Ryugu with anhydrous spectra exhibit different strengths in the 2-μm band absorption [28] indicates that Ryugu has gone through a collisional evolution track different from that of Bennu and perhaps also has a different original parent body. The possible minor presence of bright materials in returned sample may provide a key to reveal Ryugu's orbital and collisional evolution history.

Main References:

[1] Fujiwara, A. et al. The rubble-pile asteroid Itokawa as observed by Hayabusa. *Science* **312**, 1330-1334 (2006).

[2] Watanabe, S. et al. Hayabusa2 arrives at the carbonaceous asteroid 162173 Ryugu—A spinning top–shaped rubble pile. *Science* **364**, 268-272 (2019).

[3] Lauretta, D. S. et al. The unexpected surface of asteroid (101955) Bennu. *Nature* **568**, 55 (2019).

[4] Sugita, S. et al. The geomorphology, color, and thermal properties of Ryugu: Implications for parent-body processes. *Science* **364**, eaaw0422 (2019).

[5] Kitazato, K. et al. The surface composition of asteroid 162173 Ryugu from Hayabusa2 near-infrared spectroscopy. *Science* **364**, 272-275 (2019).

[6] Nakamura, T. et al. Itokawa dust particles: a direct link between S-type asteroids and Ordinary Chondrites. *Science* **333**, 1113-1116 (2011).

[7] Hiroi, T. et al. Thermal metamorphism of the C, G, B, and F asteroids seen from the 0.7 μm, 3 μm, and UV absorption strengths in comparison with carbonaceous chondrites. *Meteoritics & Planetary Science* **31**, 321-327 (1996).

[8] Hiroi, T. et al. Reflectance spectra (UV-3μm) of heated Ivuna (CI) meteorite and newly identified thermally metamorphosed CM chondrites. *Lunar and Planetary Science Conference XXVII*, 551-552 (1996).

[9] Bowell, E., and Zellner, B. Polarizations of asteroids and satellites. In *Planets, stars and nebulae studied with photopolarimetry* (pp. 381-404). Univ. of Arizona Press Tucson (1974).

[10] Marty, B. et al. Origins of volatile elements (H, C, N, noble gases) on Earth and Mars in light of recent results from the ROSETTA cometary mission. *Earth and Planetary Science Letters* **441**, 91-102 (2016).

[11] Sarafian, A. R. et al. Early accretion of water in the inner solar system from a carbonaceous chondrite–like source. *Science* **346**, 623-626 (2014).

[12] Morota, T. et al., Surface evolution of C-type asteroid 162173 Ryugu revealed from global mapping and touchdown operation of Hayabusa2, *Science* (accepted).

[13] Sasaki, S. et al. Production of iron nanoparticles by laser irradiation in a simulation of lunar-like space weathering, *Nature* **410**, 555-557(2001).

[14] Michikami et al. Boulder size and shape distributions on asteroid Ryugu. *Icarus* **331**, 179-191 (2019).

[15] Michikami et al. Fragment shapes in impact experiments ranging from cratering to catastrophic disruption. *Icarus* **264**, 316-330 (2016).

[16] Bus, S. J. and Binzel, R. P. Phase II of the small main-belt asteroid spectroscopic survey: A feature-based taxonomy. *Icarus* **158**, 146-177 (2002).

[17] Nakamura, T. et al. Post-hydration thermal metamorphism of carbonaceous chondrites. *Journal of Mineralogical and Petrological Sciences* **100**, 260-272. (2005)

[18] Applin, D. M. et al. Ultraviolet spectral reflectance of carbonaceous materials. *Icarus* **307**, 40 – 80. (2018).

[19] Grimm, R. E. and McSween Jr, H. Y. Water and thermal evolution of carbonaceous chondrite parent bodies. *Icarus* **82**, 244-280 (1989).

[20] Mainzer, A. et al. NEOWIDE observations of near-Earth objects: preliminary results. *The Astrophysical Journal* **743**, 156 (2011).

[21] DeMeo, F. and Carry, D. Solar System evolution from compositional mapping of the asteroid belt. *Nature* **505**, 629-634 (2014).

[22] Campins, H. et al. The origin of asteroid 162173 (1999 JU3). *The Astronomical Journal* **146**, 26 (2013).
[23] Cellino, A. et al. The puzzling case of the Nysa–Polana family. *Icarus* **152**, 225-237 (2001).
[24] Bottke Jr, W. F. et al. Velocity distributions among colliding asteroids. *Icarus* **107**, 255-268 (1994).
[25] Bottke Jr, W. F. et al. The fossilized size distribution of the main asteroid belt. *Icarus* **175**, 111-140 (2005).
[26] Jutzi, M. et al. Fragment properties at the catastrophic disruption threshold: The effect of the parent body's internal structure. *Icarus* **207**, 54-65 (2010).
[27] Campins, H. et al., The origin of asteroid 101955 (1999 RQ_{36}). *The Astrophysical Journal Letters* **721**, L53 – L57 (2010).
[28] DellaGiustina, D. et al., Material from (4) Vesta on Asteroid (101955) Bennu. *Nature Astronomy* (in revision).

Acknowledgements:
The Hayabusa2 spacecraft was developed and built under the leadership of JAXA, with contributions from DLR and CNES, and in collaboration with NASA, Nagoya Univ., Univ. of Tokyo, NAOJ, Univ. of Aizu, Kobe Univ., and other universities, institutes, and companies in Japan. We also thank many engineers, including Noriyasu Inaba of JAXA and Tetsuya Masuda, Seiji Yasuda, Kouta Matsushima, and Takeshi Ohshima of NEC Corp. for their dedicated work on the Hayabusa2 mission, Koshi Sato at NEC Corp. for ONC development, and Shingo Kashima at NAOJ for optical calculations. Funding: ET acknowledges financial support from the project ProID2017010112 under the Operational Programmes of the European Regional Development Fund and the European Social Fund of the Canary Islands (OP-ERDF-ESF), as well as the Canarian Agency for Research, Innovation and Information Society (ACIISI). SW, TMo, MAr, TO, TN, NN, MAb, SSa, and SSu were supported by KAKENHI from the JSPS (Grant Nos. 17H06459, 19H01951, 16H04044, 19K03958, and 18H01267) and the JSPS Core-to-Core program "International Network of Planetary Sciences". TH acknowledges funding support from NASA Emerging World/Planetary Data Archiving and Restoration. DD acknowledges funding through the NASA Hayabusa2 Participating Scientist Program (grant number NNX16AL34G), and NASA's Solar System Exploration Research Virtual Institute 2016 (SSERVI16) Cooperative Agreement (NNH16ZDA001N) for TREX (Toolbox for Research and Exploration). PM and MAB acknowledge funding support from the French space agency CNES. PM also acknowledges funding from Academies of Excellence: Complex systems and Space, environment, risk, and resilience, part of the IDEX JEDI of the Université Côte d'Azur.

Author contributions:
E.T. coordinated coauthor contributions, led the ONC data analyses and interpretations.; ONC data acquisitions and reductions: R.H., N.S., Y.Yo., M.Y., S.Su., T.Mo., S.Ka. H.Sa., M.M., T.K., E.T., C.Ho., K.O., H.Su., M.I., K.Yoshio, M.H, Y.C., C.S., and M.S.; NIRS3 data acquisitions and reductions: L.R., K.K., C.P., T.I., M.Ab. and M.Oh.; Shape modeling and spacecraft trajectory: N.H.(Kobe), N.H.(Aizu). And Y.Ya.; Science operations of spacecraft: S.Tan., F.T., S.N., S.K., T.Y., N.O., G.O., Y.M., K.Yoshik., T.T., Y.Ta., A.F., H.T., Y.Ya., T.O., M.Y., Y.S., K.S., N.H.(Kobe), Y.I., K.O., C.H., S.H., O.M., H.S., T.Sh., S.So., R.T., T.I., M.H., H.Y., M.Oz., M.Ab., M.Yo., T.Sa., S.W., and Y.Ts.; Project administration: Y.Ts., S.W., M.Yo., T.Sa., S.Tan., F.T., S.N., Y.Ya., K.K., S.Su., N.N., M.Ab., S.Tac, M.Ar., H.I., M.I., and K.W.; Interpretation and writing

contribution: E.T., C.S., L.R., T.N., S.Su., T.Mo., M.P., M.M., S.W., T.H., M.T., N.S., D.D., M.A.B., P.M., H.Y. and J.d.L. All authors discussed the results and commented on the manuscript.

Main figure legends

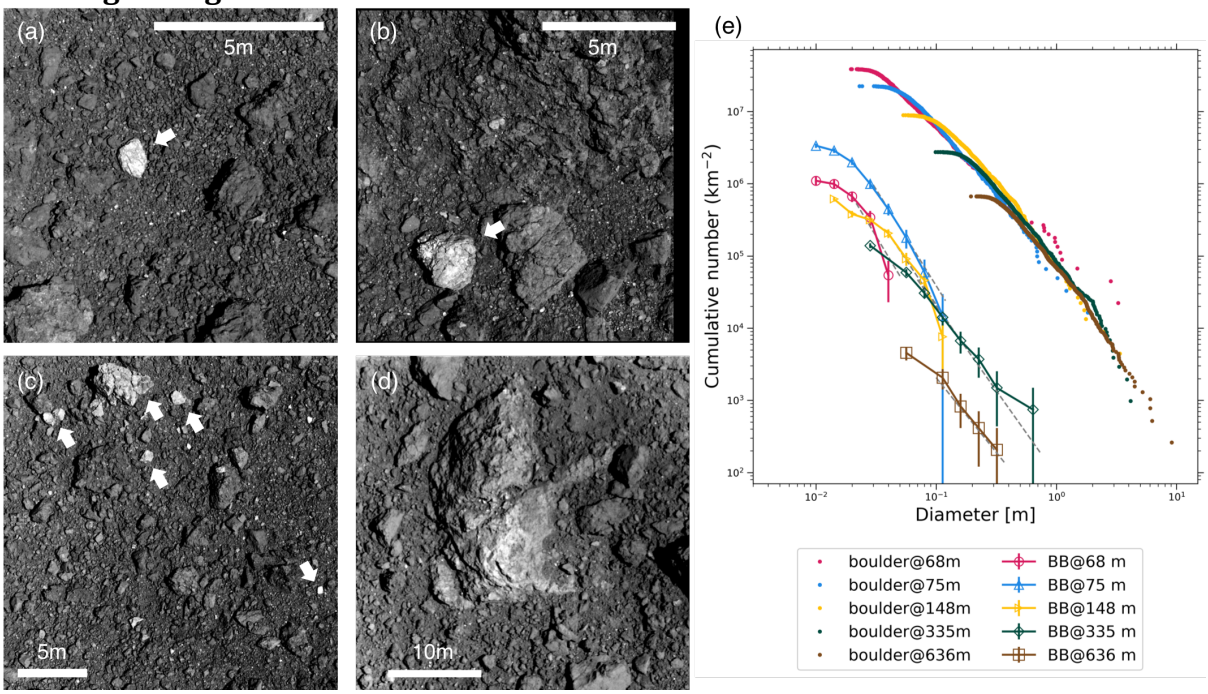

Figure 1. Bright boulders observed by ONC-T. (a) hyb2_onc_20190221_215938 (10 mm/pixel), (b) hyb2_onc_20190221_215222 (13 mm/pixel), (c) hyb2_onc_20190221_213610 (25 mm/pixel), (d) The largest bright boulder (M6) during the SCI deployment operation: 07902_20190420130002 (48 mm/pixel). (e) Cumulative size distribution *N(>D)* of bright boulders (BB) from different image resolutions (dashed lines) compared with that of general boulders (dotted) in [14] during the MINERVA-II deployment operation. Same color plots are derived from the same image. The gray dashed lines indicate the power law fits to the boulder counts. The cumulative size distribution power-index $\alpha > 2$ is consistent with that of the size distribution of fragments produced by catastrophic disruption [SM2].

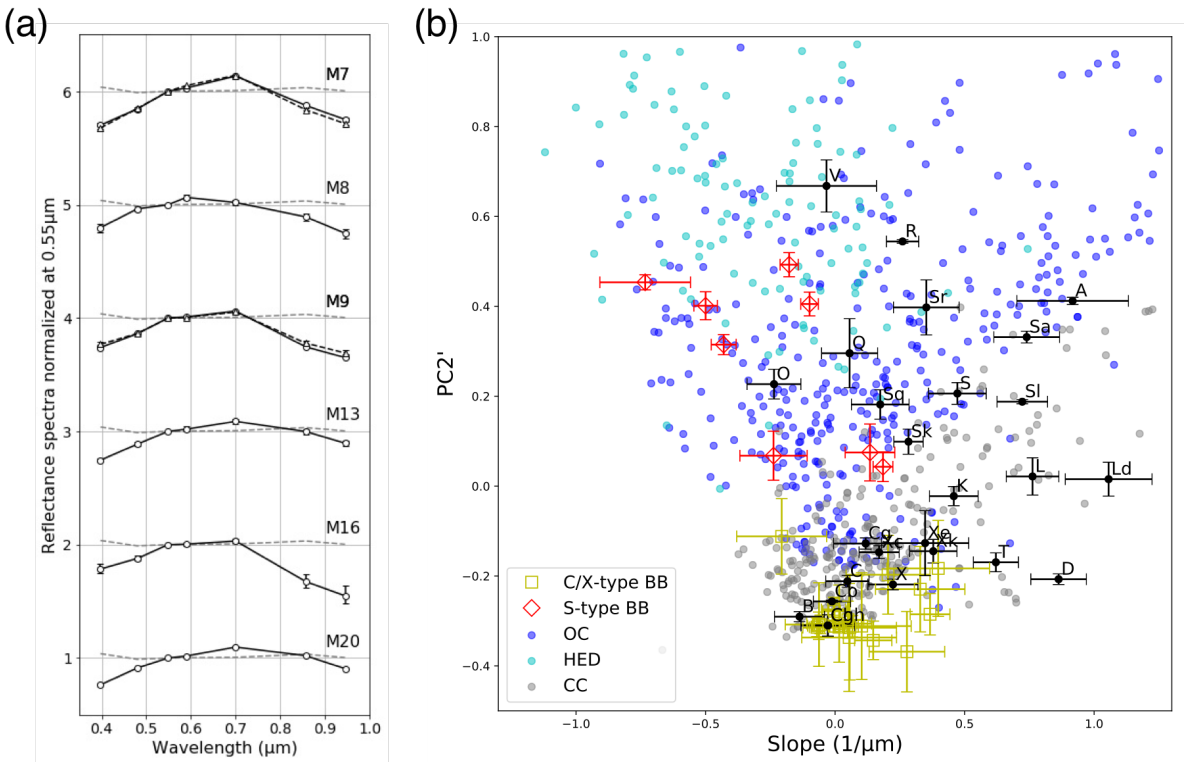

Figure 2. Visible spectral variety of S-type bright boulders. (a) Spectra of the S-type bright boulders normalized at 0.55 μm. They are offset by 1 for clarity. (b) Visible spectral slope (0.40 μm (ul) to 0.95 μm (p)) and PC2' diagram used for classification of the bright boulder spectra [Supplementary Information]. The index PC2' was defined from the principal component analysis on the main belt asteroids indicating an absorption towards 1 μm [16]. S-type bright boulders have positive PC2' values representing the absorption towards 1 μm. Color comparison of bright boulders (S-types: red diamonds, C/X-types: yellow squares) with taxonomy classes [16] (black dots) and laboratory measured meteorite spectra (OCs: blue dots, HEDs: light blue dots, and carbonaceous chondrites: gray dots) [Supplementary Information] are also shown in this space. Meteorite samples are distributed over a large area. S-type bright boulders are well inside of these HED and OC meteorite distributions.

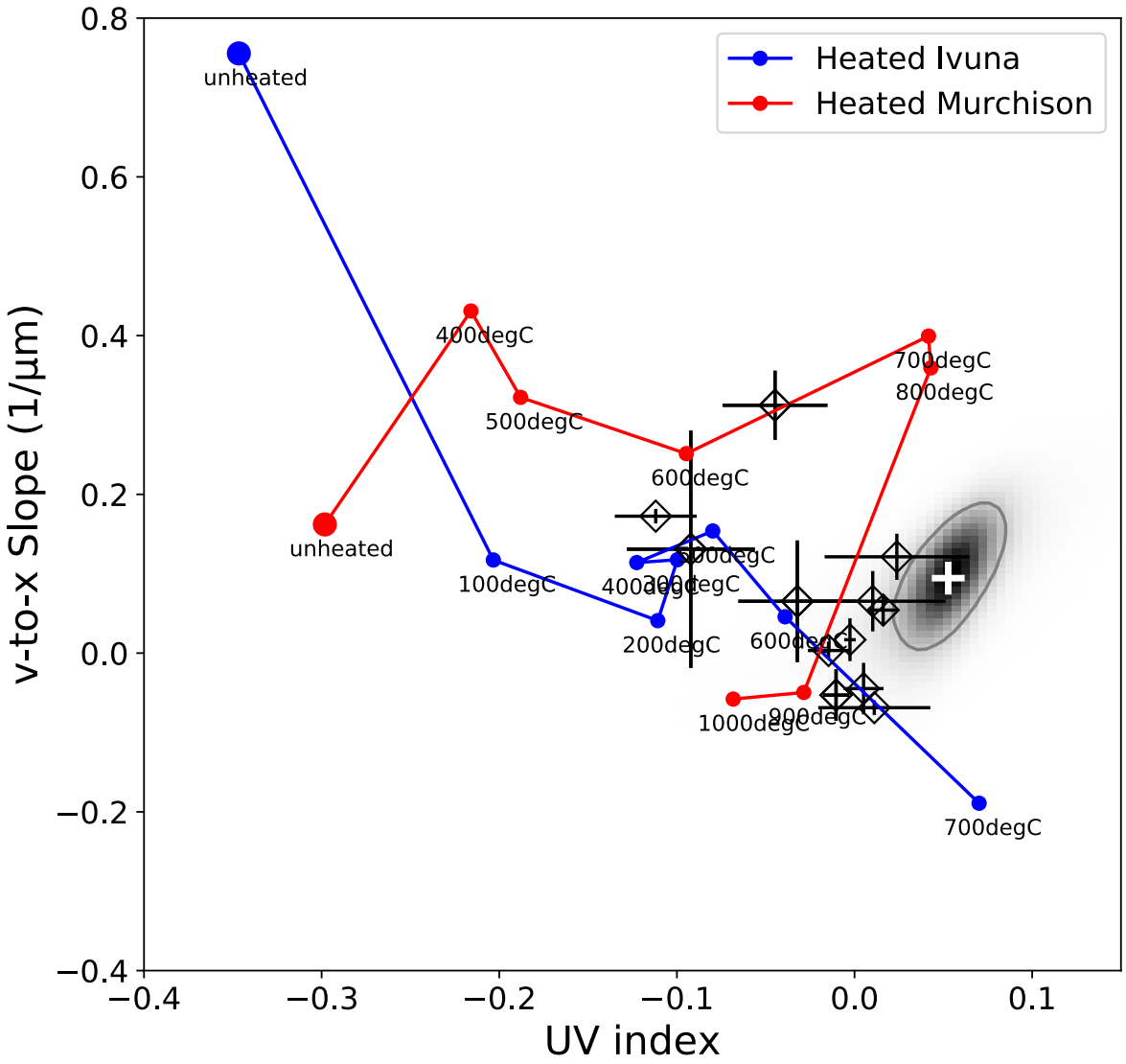

Figure 3. Visible spectral variety of C/X-type bright boulders. C/X-type bright boulders (black diamonds) compared with the heating experiments on carbonaceous chondrites (Ivuna: blue and Murchison: red) [7, 8] in the spectral slope from 0.55 to 0.86 μm (v-to-x slope) and the ultraviolet (UV) index (the upturn of ul-band (0.40 μm) compared with the continuum line defined by v-to-x slope) space. Black cloud describes the deviation of the global spectra of Ryugu from the home position (~20km) observation, which is slightly shifted towards more UV up-turn. The gray line shows the 1-sigma (68% probability) of spectral distribution and the white cross indicates the average spectrum of Ryugu.

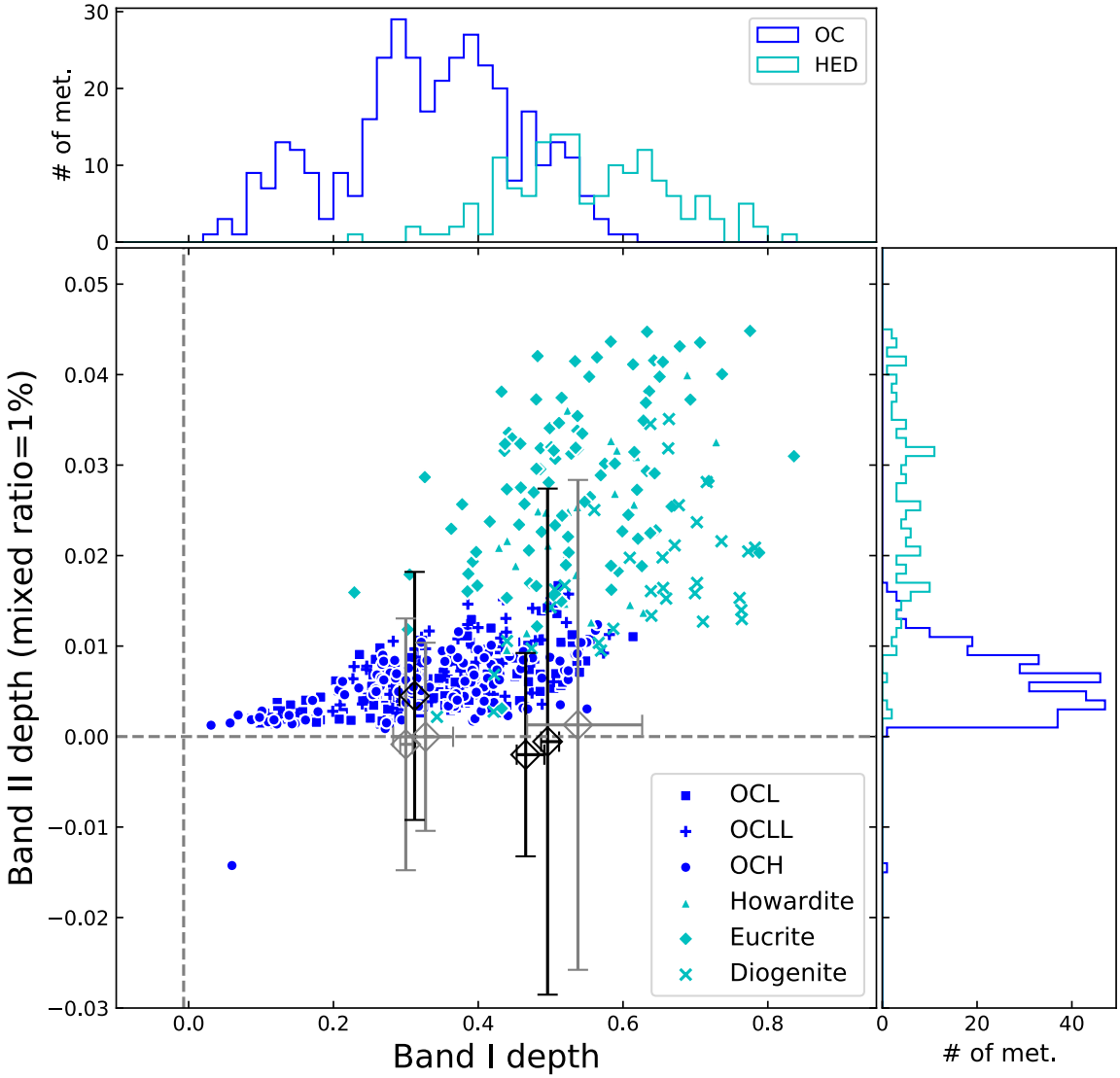

Figure 4. S-type bright boulders absorptions at p-band (0.95 μm), Band I depth, observed by ONC-T and 2-μm band depth , Band II depth, observed by NIRS3. The Band I depth is absorption at p band (0.86 μm) based on the extrapolated value from v-to-w (0.55 to 0.70 μm) slope. The Band II depth of a bright boulder is determined from the NIRS3 spectra after normalization with a spectrum of adjacent area. The band II depth is defined as the absorption at 2 μm from the continuum defined by the interpolation of the normalized reflectance at 1.8 μm and 2.5 μm. Bright boulders occupying ≳1% of the NIRS3 footprint are shown in black diamonds and those occupying ≲ 0.5% are shown in gray diamonds. To compare those spectra with the small occupancy of the bright boulder in the footprint area, the laboratory measured meteorite spectra (OCL: L chondrite, OCLL: LL chondrite, OCH: H chondrite, and HEDs) [Supplementary Information] are linearly mixed with the average Ryugu spectrum, assuming the area of meteorites is 1% of the spectrometer footprint. The dashed line indicates the Ryugu average absorption. Histograms show the distribution of meteorites along both axes. HEDs are scatter large area of band II depth, while OCs shows peak around 0.6%.

Methods

1. ONC-T data processing

Calibration and extraction of spectral shape and albedo

The ONC-T images are calibrated from digital number to radiance factor using the same method described in [29] using the updated flatfields derived by [30]. Owing to the rotation of the asteroid during an image sequence acquisition over a seven-band observation, the position of bright boulder (BB) in the FOV changes slightly over time. The illumination and observation geometrical information are derived by SPICE toolkit based on the shape model and SPICE kernels. Rotational effect results in sub-degree (< 0.2°) differences in phase angle (i.e., spacecraft–bright boulder–Sun angle) between different bands. Considering this effect, images were photometrically corrected to incidence (i), emission (e), and phase angles (α) of 30°, 0°, and 30°, respectively, based on the Hapke disk-resolved model [31] in the supplementary online material of [4].

Objects smaller than the diameter of 3 pixels cannot be evaluated directly from the image because the point spread function (PSF; FWHM∼1.7 pixels, [32]) blurs the radiance from the BB. The radiances from the BB and adjacent area are contaminated. In that case, we need to remove the radiance of the adjacent area from the radiance measurement of the BB (i.e., similar to the point source stellar radiance measurement). Thus, we measured the spectra in either of two ways depending on the size of BBs. 1) For BBs with a diameter >3 pixels, we acquired spectra of BBs by directly averaging the surface spectra. Specifically more than 15 pixels[2] for each BB in each band are averaged in this study. 2) For BBs with diameter ≦ 3 pixels, we subtracted the contributions from the adjacent area (labeled background) to the BB, from the total radiance of the BB area (ROI_A in Supplementary Figure 1). Using the estimated area S, the radiance of the BB I_{BB} is calculated by

$$I_{BB} = \frac{I_{ROI_A} - I_{background}}{S} \qquad \text{(S1)}$$

where I_{ROI_A} is the total radiance in ROI_A and $I_{background}$ is the estimated total radiance of the background. $I_{background}$ is estimated from the surrounding area near the ROI_A (ROI_B in Supplementary Figure 1); $I_{background} \sim \frac{I_{ROI_B}}{R^2 - r^2}(r^2 - S)$, where *r=7* pixels and *R=21* pixels are the size of ROI_A and ROI_B, respectively. And the normalized spectrum is obtained by

$$\bar{I}_{BB} = \frac{I_{BB}}{I_{BB,v}} = \frac{I_{ROI_A} - I_{background}}{I_{ROI_A,v} - I_{background,v}}, \qquad \text{(S2)}$$

where the subscript v indicates the value for v band.

Normal albedo was measured with same way as Eq. (S1) but using the images photometrically corrected to (i, e, α) = (0°, 0°, 0°).

Extended Figure 6 shows the locations and sizes of the BBs found in the images from the MASCOT hovering operation conducted on 3 to 4 October 2019 at the altitude of ∼3 km. Extended Figures 1 and 2 show morphologies and spectra of the BBs. The BBs with diameter ≲ 1 m in Extended Figure 6 are measured by the method #2.

Selection Methodology

Bright boulders are identified as areas with peak normal albedo values >1.5 times than Ryugu's globally averaged albedo, with a peak normal albedo >6.8%. For a boulder to be designated as a bright boulder at least 4 adjacent pixels meeting this brightness

criteria was required, eliminating false identifications due to pick up noise or cosmic rays. The standard deviation in normal albedo across Ryugu's surface is ± 4.1 – 5.0%. The selected normal albedo threshold for bright boulders is well outside this deviation and is distinctly represents an anomalous value.

We tested the robustness of the threshold for detecting bright boulders. If we set the threshold to 1.6 times the global average, we also found both S- and C/X-type bright boulders. However, we could not detected bright boulder M20 due to its small size, while we could identify bright boulders M1, M11, and M5. The reason M20 was not detected is that our detection criteria require more than four adjacent pixels exceed the threshold. Thus, the choice of brightness threshold does not influence the *spectral type* of bright boulder detected, but limits the *size* of bright boulders that can be detected.

If we set the threshold to 1.4 times the global average we find ~30 more C/X-type bright boulders. The albedo and spectral variety of C/X-type bright boulders are along a continuous range from Ryugu's average, thus it is difficult to distinguish bright boulders if the threshold is set too low. With too low a threshold the photometric error in the derived normal albedo values does not provide a 1 sigma deviation from the global average. The threshold value needs to provide a clear difference between bright boulders and general boulders. A threshold of 1.5 times the global average albedo tested to be the best value to identify anomalously bright boulders.

It is important to note that classification of a boulder as a 'bright boulder' is based solely on its albedo compared to the global average albedo. The classification into S-type bright boulder and C/X-type bright boulder is based on spectral properties after it has been identified as a bright boulder.

Classification of bright boulders

Based on the taxonomy by [33], we decomposed the spectra of BBs with the same basis vectors, spectral slope and PC2'. The SMASS2 spectral data are available through PDS website (https://sbn.psi.edu/pds/resource/smass2.html, [34]). PC2' was obtained from principal component analysis of SMASS2 after each spectrum was normalized by its fitted slope (Supplementary Figure 4). Component PC2' is sensitive to the strength of the 1-μm band absorption and PC3' is sensitive to the combination of the strength of UV absorption and the 0.7-μm band absorption. Note that because our spectra were obtained using broad band filters, the spectra of BBs are interpolated with a spline fitting before principal component decomposition. Within spectral slope and PC2' space, two distinct grouping of asteroids were suggested [33]; the structures were defined as S- and C/X-classes. Taxonomic classification defined by [33] is shown in the Fig. 2. Six BBs with PC2' value greater than 0, correspond to deeper 1-μm absorption, are classified as S-type BBs and others as C/X-type BBs.

Color indexes

Spectral slope:

Similar to [33], the 7-band or 4-band spectra are fitted to the equation below using the a least-squares method,

$$\bar{R}_i = 1 + \gamma(\lambda_i - 0.55),$$

where $\bar{R}_i$ is the normalized reflectance at each band (Fig. 2 with i=ul, b, v, Na, w, x, p, and Fig. 4 with i=v, Na, w, x), λ_i is the wavelength of the band in microns [Supplementary information], and γ is the slope of the fitted line, constrained to a value of unity at 0.55 μm.

UV index:
UV index is defined to measure UV up/down-turn. To consider the effect of the continuum spectral slope, we compute the UV increase/decrease from an extrapolation based on the continuum spectral slope. That is the extrapolated reflectance $\bar{R}_{ul_0}$ at ul band from the v-to-x slope is calculated first and the UV index C_{UV} is defined as

$$C_{UV} = \frac{\bar{R}_{ul}}{\bar{R}_{ul_0}} - 1.$$

Thus, when the C_{UV} is positive, the spectrum has a UV up-turn, and vice versa.

Band I depth:
Band I depth is defined to measure the absorption towards 1-μm. To consider the effect of the continuum spectral slope, we compute the p-band increase/decrease from an extrapolation based on the continuum spectral slope. That is, the extrapolated reflectance $\bar{R}_{p_0}$ at p band from the v-to-w slope is calculated first and the Band I depth C_{bandI} is defined as

$$C_{\mathrm{bandI}} = 1 - \frac{\bar{R}_p}{\bar{R}_{p_0}}.$$

Thus, when the larger the value of C_{bandI}, the deeper the 1-μm band depth , and vice versa.

2. Size distribution of bright boulders

We analyzed the same five images used in [14] which measured all the boulder size distribution including BBs in the images [14]. We picked up the BBs brighter than 1.5 times the median value for each images (Extended Figure 3). The circular shape of BBs is assumed to calculate the diameter, i.e., the diameter D_{BB} is converted from pixel area S_{pix} as

$$D_{BB} = \sqrt{\frac{S_{pix} l^2}{2\pi}},$$

where l (m/pixel) is the pixel scale at the altitude of observation. The cumulative number distribution of boulder size can be expressed by $N(>D) \propto D^{-\alpha}$, where D is diameter of the BB, and α is the power-law index. The boulder size distribution in each image is fitted by a power-law based on the maximum likelihood method with goodness-of-fit test based on the Kolmogorov-Smirnov statistic [35] which is implemented in the python library, powerlaw, by [36]. We utilized this python library and found the power-law index for datasets in Extended Figure 7. The power-law index value for BBs is similar value to that for all boulders by [14] within the error bars except for the image at the altitude of 65 m. Because in this image apparently, several meter-scaled boulders occupy a large part of the FOV (Extended Figure 3(e)), only a little substrate could be observed. This small area may affect the BB statistics. This similarity in power-law index suggests that the BBs and other boulders could be originated from the same mechanism. Area ratio between all boulders and BBs are derived from the comparison between the intercept of cumulative number distributions of boulders from [14] and BBs counted in this study. Based on the

image at altitude of 636 m comparison of boulder number at D=0.3 m gives an area ratio of 0.03%, and based on the image at altitude of 75 m comparison of boulder number at D=0.07 m gives an area ratio of 1%.

3. NIRS3 data processing

We use calibrated NIRS3 spectra acquired between 30 June 2018 and 28 February 2019 to characterize the BBs detected by the ONC visible camera. The calibration steps for NIRS3 spectra are summarized in [37] and [5]. The raw data is calibrated using a transfer function that was computed from the on-ground calibration of the instrument [37]. The obtained radiance is defined as follows:

$$L(\lambda,T) = r(\lambda) \times \frac{F_{sun}(\lambda) \times cos\,(i)}{\pi D^2_{sun-Ryugu}} + \varepsilon(\lambda) \times \frac{2hc^2}{\lambda^5} \times \frac{1}{e^{(\frac{hc}{\lambda k_B T})} - 1} \qquad \text{(S3)}$$

where $r(\lambda)$ is the reflectance, $F_{sun}(\lambda)$ the sun incident flux, i the incidence angle and $\varepsilon(\lambda)$ the surface emissivity that is estimated around 1.87 μm. The temperature is retrieved at every location (e.g. for every spectrum), using the Planck function (Eq. (S3)). The obtained reflectance $r(\lambda)$ is then corrected to standard viewing geometry, incidence, emission, and phase angles of 30°,0°, and 30°, respectively.

We show in this paper the results for six S-type BBs (Fig. 4). Supplementary Table 1 summarizes the NIRS3 data used in this study. Here we describe the analysis of NIRS3 spectra on one of the largest BBs, M13, as an example. The characterization process is as follows: (1) we search for all NIRS3 spectra that overlap the BB longitude and latitude at ± 1°; (2) for each day of observation we extract spectra including the BB and spectra excluding the BB to enable comparison. For M13, we find 8 NIRS3 observations that including it, corresponding to a total of 57 spectra (Supplementary Figure 5).

The NIRS3 instrument presents a rather low resolution compared to the size of the bright boulder (< 3 m). Therefore, for the in-depth characterization, we use the spectra of highest resolution ~6 m x 6 m (7 August 2018). We found 14 spectra that overlap the BB and 32 spectra in the vicinity of the BB (± 5°) for comparison (Supplementary Figure 5c). From those spectra, we computed an average spectrum including M13 (from the 14 blue squares on Supplementary Figure 5c) and an average spectrum excluding M13 (from the 32 yellow squares on Supplementary Figure 5c). There is small variation within those spectra normalized at 2.5 μm. As a result, we also computed error bars for the average spectra by calculating the standard deviation of the normalized reflectance amongst the set of used spectra for both spectra including BB ('in') and adjacent areas ('out') (Extended Figure 4). We observe very slight differences in albedo level between the spectra including and excluding M13 at all resolution (Supplementary Figure 5a). Because the differences in absolute reflectance observed at high resolution may result from shadowing effects which can easily change the reflectance by 10% due to the variation in illumination conditions, we used normalized spectra to evaluate the absorption band. We performed spectral ratio to compare the average normalized spectrum 'in' with the average normalized spectrum 'out' and highlight spectral shape difference (Extended Figure 4). The error bars are calculated from the law of propagation of error as indicated below:

$$\frac{(\bar{R}_{in} \pm \sigma_{in})}{(\bar{R}_{out} \pm \sigma_{out})} = \frac{\bar{R}_{in}}{\bar{R}_{out}} \pm \sqrt{\left(\frac{\sigma_{in}}{\bar{R}_{out}}\right)^2 + \left(\frac{\bar{R}_{in}}{\bar{R}_{out}^2}\sigma_{out}\right)^2},$$

where $\bar{R}_{in}$ and $\bar{R}_{out}$ are the average normalized reflectance spectra 'in' and 'out', respectively, and σ_{in} and σ_{out} are the corresponding standard deviations.

For the calculation of the Band II depth $d_{2.0}$, as summarized in Supplementary Table 1, we use only high resolution spectra (spot size on the surface of Ryugu < 12 m). The absorption degree $d_{2.0}$ at 2 μm is measured by computing the ratio between the reflectance at 2.0 μm to the interpolated continuum based on the reflectance at 1.8 μm and 2.5 μm.

$$d_{2.0} = 1 - \frac{0.7\bar{R}_{2.0}}{0.5\bar{R}_{1.8} + 0.2\,\bar{R}_{2.5}}$$

where the R_{wl} is the reflectance ratio at wl=1.8, 2.0, and 2.5 μm. The error in absorption is given by the standard deviation between multiple observations on each site.

4. Collision on Ryugu with an ordinary chondrite

One possible explanation for the exogeneous materials is that they fall with a slow velocity so that they do not disrupt on collisions to Ryugu. Here we estimate the peak pressure when an ordinary chondrite (OC) impacts Ryugu. Then we discuss the required condition for that type of soft-landing scenario. The peak pressure during a collision between an OC and a carbonaceous one can be calculated based on the Rankine-Hugoniot equations as:

$$P_0 = \frac{1}{2}\xi\rho_{0t}C_t^2\left(1 + \frac{1}{2}s_t\xi\frac{v}{C_t}\right)\left(\frac{v}{C_t}\right),$$

where P_0 is the initial peak pressure, ρ_{0t} is the target density, C_t and s_t are constants for the Hugoniots state curve, and v is the impact speed. The parameter ξ, related to shock impedance matching, can be approximately obtained as:

$$\xi \sim 2/\left(1 + \frac{\rho_{0t}C_t}{\rho_{0i}C_i}\right),$$

where ρ_{0i} and C_i are the impactor density and the Hugoniot parameter for the impactor, respectively. The parameters for the Hugoniot state curve, C and s, were measured by [38] for the CM2 chondrite Murchison (C=1.87±0.07 km/s, s=1.48±0.03) and the L6 chondrite Bruderheim (C=3.11±0.06 km/s, s=1.62±0.02). Therefore, the peak pressure can be estimated as in Extended Figure 5. Comparison with the compressive strength of OC is used to estimate the speed of the impactor allowing its survive at impact. The compression strength of OCs was obtained to be 164 ± 106 Mpa based on a compilation of 22 measurements in the literature [39]. The impactor hardly survives at impact speeds ≥ 0.2 km/s. Thus, exogeneous materials must have collided on Ryugu at speeds < 0.2 km/s, unless they are fragments of a much larger impactor. Furthermore, if the impact speed is > 0.2 km/s, the mass of the largest fragment is < 1% of the mass of original projectile [40]. This suggests that if the BBs larger than 0.5 m were the fragments of a larger impactor with higher velocity, the impactor should be larger than 50 m. However, a 25-m-sized projectile can catastrophically disrupt Ryugu, assuming Q_D*~250 J/kg for non-porous material [41] and Q_D*~800 J/kg for porous material [26], where Q_D* is so-called catastrophic specific impact energy threshold which results in the fragmentation and escape of half of the target mass. Thus, if the exogeneous materials are accumulated on Ryugu by collision during its post-formation evolution, slow collisions < 0.2 km/s are needed.

Data and materials availability:
All images and input data used in this study are available at the JAXA Data Archives and Transmission System (DARTS) at www.darts.isas.jaxa.jp/planet/project/hayabusa2/Tatsumi_2020, and higher-level data products will be available in the Small Bodies Node of the NASA Planetary Data System (https://pds-smallbodies.astro.umd.edu/) 1 year after mission departure from the asteroid.

Reference for methods:

[29] Tatsumi, E. et al., Updated inflight calibration of Hayabusa2's optical navigation camera (ONC) for scientific observations during the cruise phase. *Icarus* **325**, 153-195 (2019a).

[30] Tatsumi, E., et al., Updated flat-fields of ONC-T/Hayabusa2 based on close encounter with Ryugu. *50th Lunar and Planetary Science Conference*, #1745 (2019b).

[31] Hapke, B., Bidirectional reflectance spectroscopy: 1. Theory. *Journal of Geophysical Research* **86**, 3039–3054 (1981).

[32] Kameda, S. et al., Preflight Calibration Test Results for Optical Navigation Camera Telescope (ONC-T) Onboard the Hayabusa2 Spacecraft. *Space Science Reviews* **208**, 17-31 (2017).

[33] Bus, S. and Binzel, R.P., Phase II of the Small Main-Belt Asteroid Spectroscopic Survey. *Icarus* **158**, 146 – 177 (2002).

[34] Bus, S. and Binzel, R. P., Small Main-belt Asteroid Spectroscopic Survey, Phase II. EAR-A-I0028-4-SBN0001/SMASSII-V1.0. NASA Planetary Data System (2003).

[35] Clauset, A., et al., Power-law distributions in empirical data. *SIAM Review* **51**, 661-703 (2009).

[36] Alstott, J. et al., Powerlaw: a Python package for analysis of heavy-tailed distributions. arXiv: 1305.0215 (2014).

[37] Iwata, T. et al., NIRS3: The Near Infrared Spectrometer on Hayabusa2., *Space Science Review* **208**, 317-337 (2017).

[38] Anderson, W. W. and Ahrens, T. J., Shock Wave Equations of State of Chondritic Meteorites. *AIP Conference Proceedings* **429**, 115-118 (1998).

[39] Flynn et al., Physical Properties of the Stone Meteorites: Implications for the Properties of Their Parent Bodies. *Chemie der Erde* **78**, 269-298 (2018).

[40] Fujiwara, A., and Tsukamoto, A., Experimental study on the velocity of fragments in collisional breakup. *Icarus*, **44**(1), 142-153 (1980).

[41] Benz, W. and Asphaug, E., Catastrophic disruptions revisited. *Icarus* **142**, 5-20 (1999).

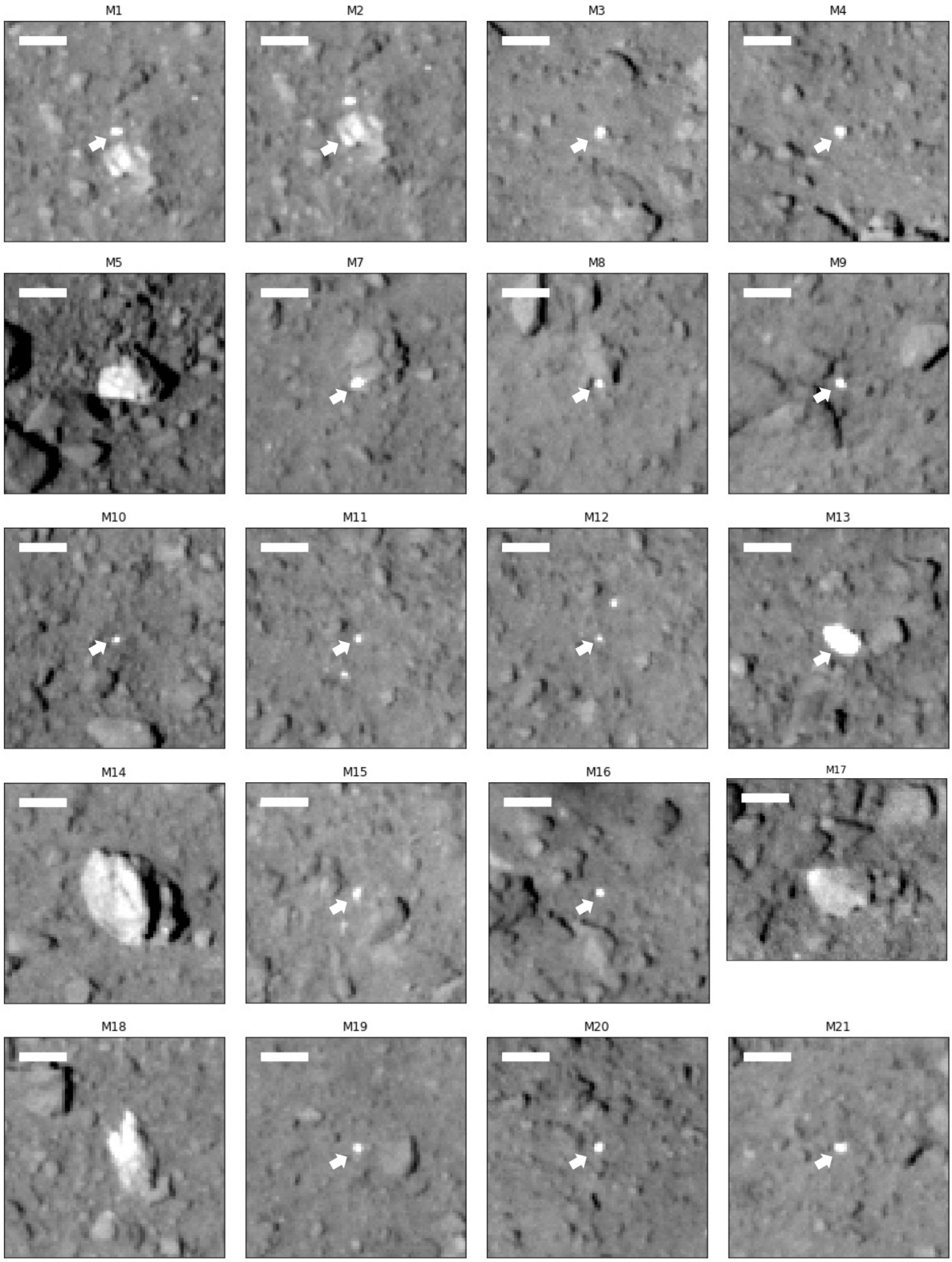

Extended Data Fig.1 Bright boulder morphologies. The resolutions of these images are 0.28–0.30 m/pixel, as listed in Extended Data Fig. 4. Scale bars in the images are 5 m. M6 is shown in Fig. 1 of the main text.

Image	Altitude (m)	Counted number of bright boulders	Power-index α	Error of α	Fitted size range (m)	Power-law index in Michikami et al. (2019)
hyb2_onc_20180921_043010_tvf	636	22	2.07	0.65	0.10-0.38	2.07 ± 0.05
hyb2_onc_20180921_041826_tvf	335	187	2.35	0.30	0.07-0.73	2.01 ± 0.06
hyb2_onc_20180921_034938_tvf	148	161	2.48	0.34	0.04-0.14	1.96 ± 0.07
hyb2_onc_20180921_040154_tvf	75	368	2.37	0.33	0.03-0.12	1.98 ± 0.09
hyb2_onc_20180921_040634_tvf	65	101	2.77	0.46	0.02-0.05	1.65 ± 0.05

Extended Data Fig. 2 Power index for boulder size distribution from close-up images. The power index is calculated based on the maximum-likelihood fitting method by ref. [35]. The cumulative boulder size distribution is expressed as $N(>D) \propto D^{-\alpha}$, where D is the diameter of the bright boulder, and α is the power-law index.

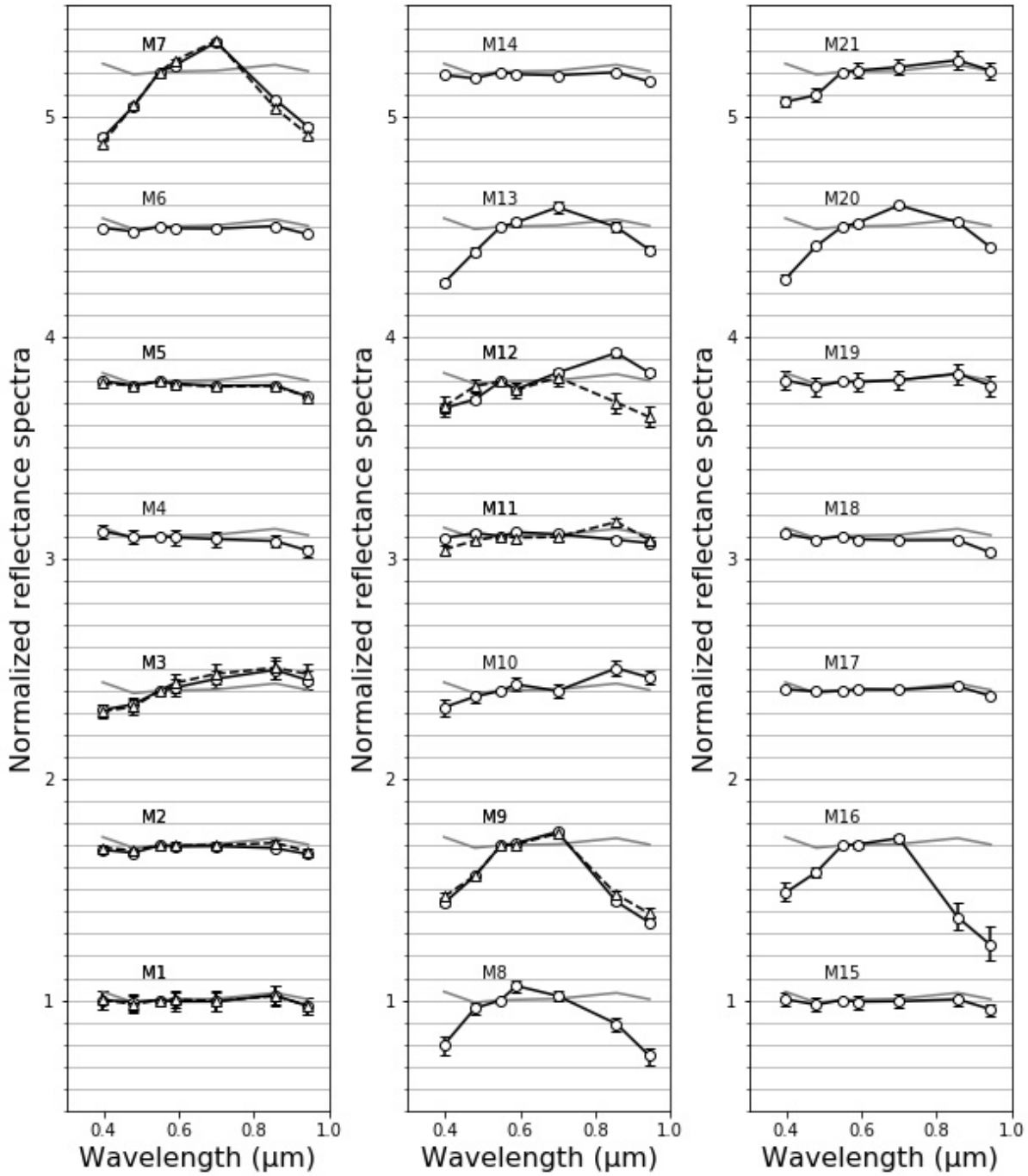

Extended Data Fig. 3 Normalized reflectance spectra of bright boulders (black lines) compared with the average spectrum of Ryugu (gray lines). Lines are offset by 0.7 for clarity. The bright boulders which display two spectra were observed twice in different multiband image sets.

ID	Latitude (°)	Longitude (°)	Pixel dimension* a (pix), b (pix)	Image resolution (m/pixel)	Diameter (m)	Average normal albedo	Type
M1	-1.98	105.07	6, 4	0.29	1-2	$6.5^{+3.0}_{-0.8}$	C/X
M2	-2.35	105.15	10, 5	0.29	~3	$6.3^{+2.9}_{-0.8}$	C/X
M3	4.68	61.61	6, 6	0.29	1-2	$5.7^{+2.6}_{-0.7}$	C/X
M4	1.57	67.07	6, 6	0.29	1-2	$5.6^{+2.6}_{-0.7}$	C/X
M5	-15.49	12.81	20, 12	0.29	~5	$6.1^{+2.8}_{-0.8}$	C/X
M6	7.19	334.53	80, 52	0.29	23	$5.7^{+2.6}_{-0.7}$	C/X
M7	-17.02	284.96	3.2, 2.8	0.29	~1	$12.2^{+5.6}_{-1.6}$	S/Q
M8	-3.16	189.93	< 2, <2	0.29	<1	N/A	S/Q
M9	-1.26	129.63	2.1, 2.6	0.28	~1	$11.1^{+5.1}_{-1.4}$	S/Q
M10	-2.55	94.13	<2, <2	0.29	<1	N/A	C/X
M11	-4.21	34.68	2.8, <2	0.29	<1	N/A	C/X
M12	-4.63	34.45	<2, <2	0.29	<1	N/A	C/X
M13	-0.68	22.12	13, 9	0.29	~3	$15.1^{+7.0}_{-2.0}$	S/Q
M14	-18.41	251.01	41, 28	0.29	~10	$5.9^{+2.7}_{-0.8}$	C/X
M15	0.05	293.57	5, 6	0.29	1-2	$5.9^{+2.7}_{-0.8}$	C/X
M16	7.63	148.84	<2, <2	0.30	<1	N/A	S/Q
M17	-26.61	14.03	25, 20	0.29	~6	$6.1^{+2.8}_{-0.8}$	C/X
M18	-7.22	339.79	32, 15	0.29	~4	$6.9^{+3.1}_{-0.9}$	C/X
M19	-7.60	306.03	5, 6	0.29	1-2	$5.9^{+2.7}_{-0.8}$	C/X
M20	5.79	259.52	2.3, 2.5	0.29	~1	$10.6^{+4.9}_{-1.4}$	S/Q
M21	-5.63	308.47	6, 4	0.29	1-2	$6.7^{+3.1}_{-0.9}$	C/X

* a is major-axis diameter and b is minor-axis diameter.

Extended Data Fig. 4 The locations and sizes of bright boulders.

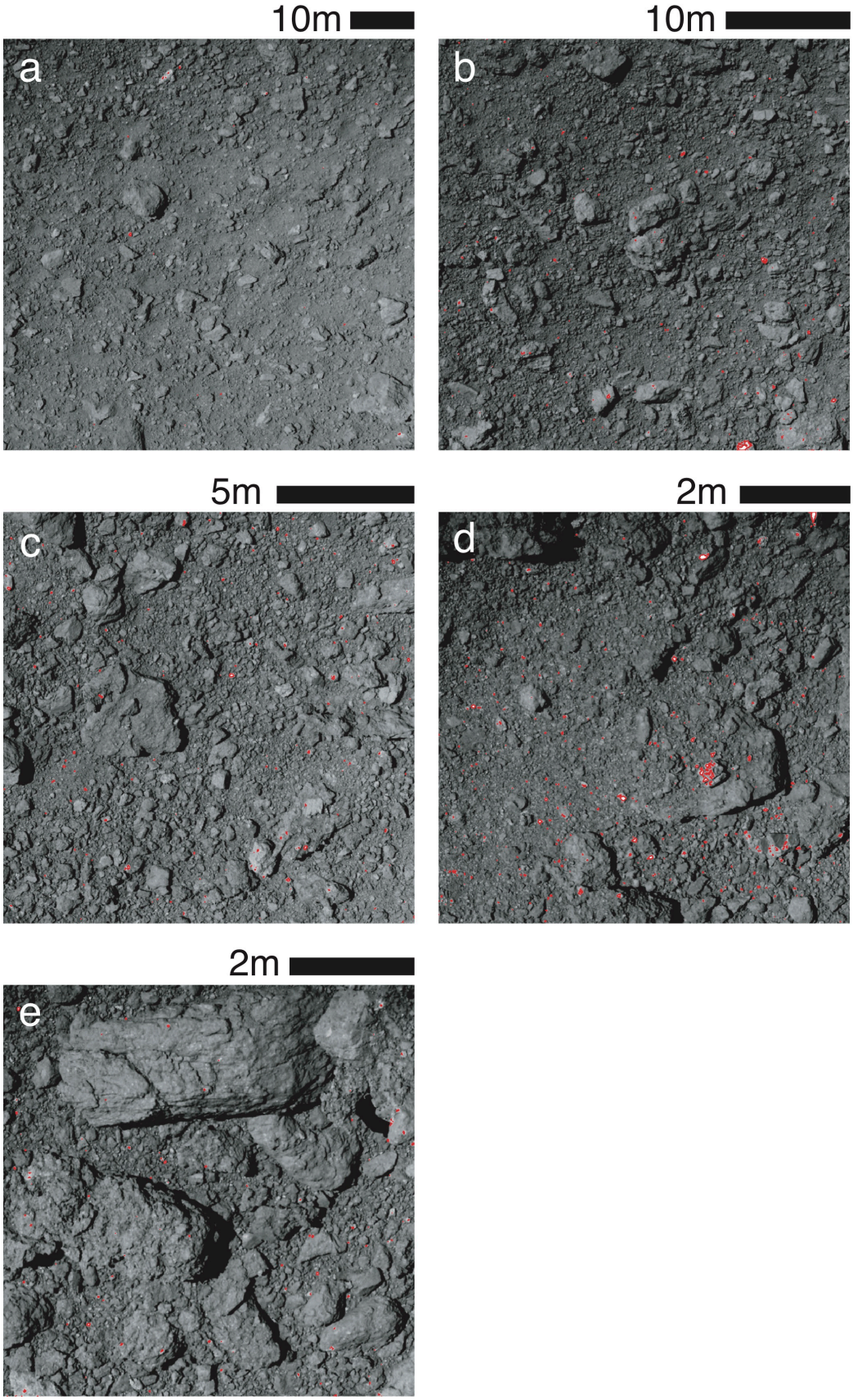

Extended Data Fig. 5 Bright boulders (enclosed by red lines) in close-up images during the MINERVA-II deployment operation on 21 September 2018. a, hyb2_onc_20180921_043010_tvf, altitude of 636 m (68 mm/pixel). b, hyb2_onc_20180921_041826_tvf, altitude of 335 m (36 mm/pixel). c, hyb2_onc_20180921_034938_tvf, altitude of 148 m (16 mm/pixel). d,

hyb2_onc_20180921_040154_tvf, altitude of 75 m (8 mm/pixel). e, hyb2_onc_20180921_040634_tvf, altitude of 68 m (7 mm/pixel).

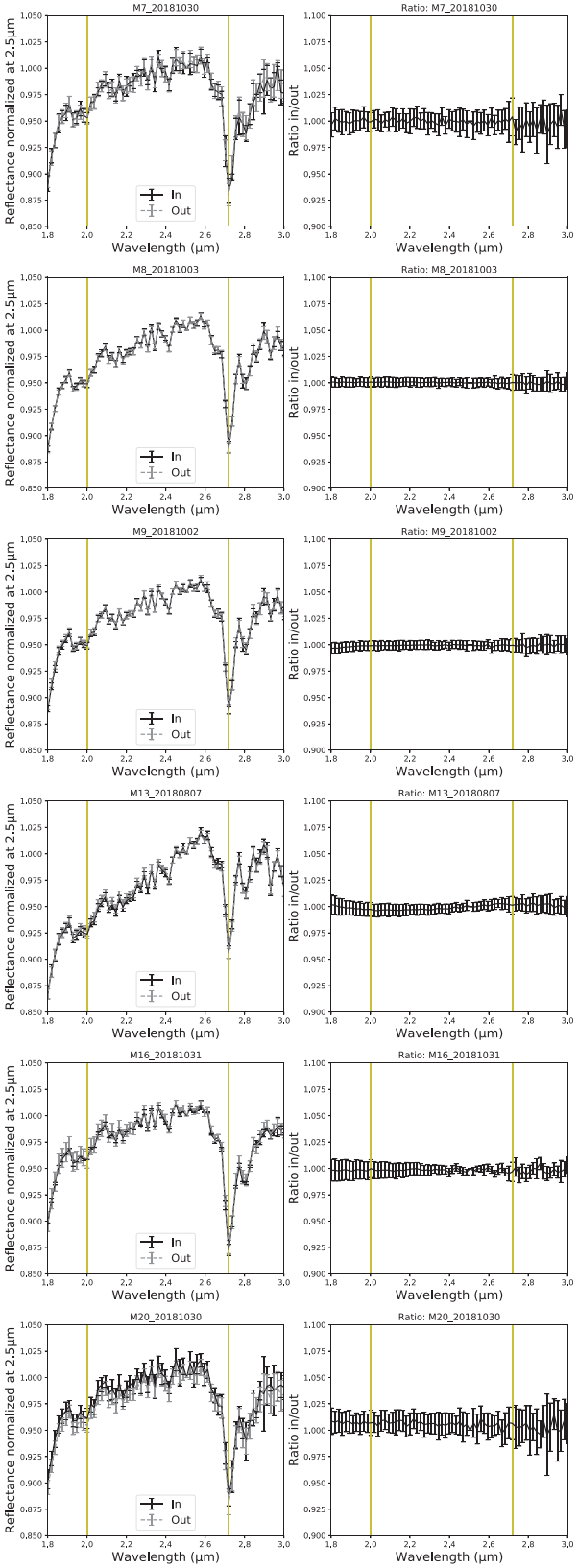

Extended Data Fig. 6 S-type bright boulders observed by NIRS3. (left) The NIRS3 spectra of the area including bright boulders (black) and adjacent areas (gray). The footprint size of NIRS3 is in Extended Table 2. (right) The normalized spectra of area including bright boulders by the adjacent areas. Only the M13 shows small absorption around 2 μm.

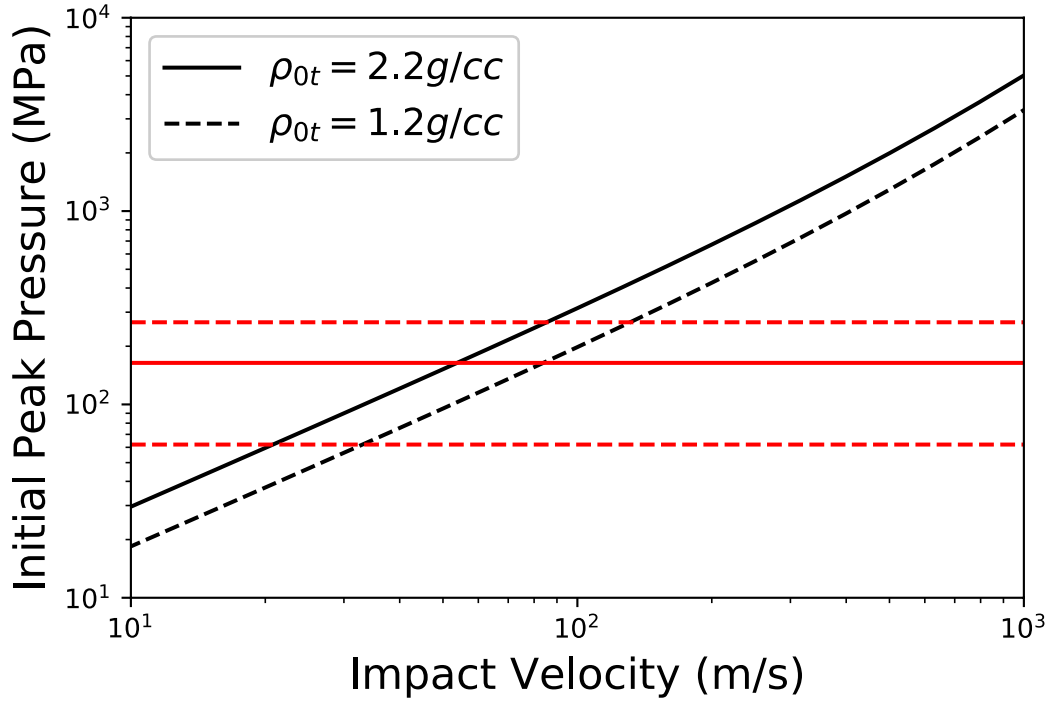

Extended Data Fig. 7 Peak pressure during a collision between an ordinary chondrite and a carbonaceous chondrite. The red solid and dashed lines indicate the average and standard deviation of compressive strength among ordinary chondrites, respectively[39]. The black solid and dashed lines indicate then peak pressure for the target densities of 2.2 g/cc and 1.2 g/cc (Ryugu bulk density), respectively.